Sub-4 nm mapping of donor–acceptor organic semiconductor nanoparticle composition

Ingemar Persson, Hugo Laval, Sylvain Chambon, Gwenael Bonfante, Kazuhiko Hirakawa, Guillaume Wantz, Benjamin Watts, Matthew A Marcus, Xiaoxue Xu, Lei Ying, et al.

Sub-4 nm mapping of donor-acceptor organic semiconductor nanoparticle composition

Ingemar Persson,[1,2] Hugo Laval,[3] Sylvain Chambon,[4] Gwenael Bonfante,[4] Kazuhiko Hirakawa,[4] Guillaume Wantz,[3] Benjamin Watts,[5] Matthew A. Marcus,[6] Xiaoxue Xu,[7] Lei Ying,[8] Girish Lakhwani,[9,10] Mats R. Andersson,[11] Julie M. Cairney,[1,11] Natalie P. Holmes[1,10,12]*

[1] Australian Centre for Microscopy and Microanalysis, University of Sydney, Sydney, NSW 2006, Australia.

[2] Thin Film Physics, Department of Physics, Chemistry and Biology (IFM), Linköping University, SE-58183 Linköping, Sweden.

[3] University of Bordeaux, IMS, CNRS, UMR 5218, Bordeaux INP, ENSCBP, F-33405 Talence, France.

[4] LIMMS/CNRS-IIS (IRL2820), Institute of Industrial Science, The University of Tokyo, 4-6-1 Komaba, Meguro-ku, Tokyo, 153-8505, Japan.

[5] Paul Scherrer Institute, 5232 Villigen-PSI, Switzerland.

[6] Advanced Light Source, Lawrence Berkeley National Laboratory, Berkeley, CA 94720, USA.

[7] School of Biomedical Engineering, Faculty of Engineering and Information Technology, University of Technology Sydney, NSW 2007, Australia.

[8] Institute of Polymer Optoelectronic Materials and Devices, State Key Laboratory of Luminescent Materials and Devices, South China University of Technology, Guangzhou 510640, P. R. China.

[9] ARC Centre of Excellence in Exciton Science, School of Chemistry, University of Sydney, Sydney, NSW 2006, Australia.

[10] The University of Sydney Nano Institute, Faculty of Science, University of Sydney, Sydney, NSW 2006, Australia.

[11] Flinders Institute for Nanoscale Science and Technology, Flinders University, Adelaide, South Australia 5042, Australia.

[12] School of Aerospace, Mechanical and Mechatronic Engineering, University of Sydney, Sydney, NSW 2006, Australia.

* Corresponding Author: natalie.holmes@sydney.edu.au

KEYWORDS: Nanomaterials, organic semiconductors, composition mapping

Abstract

We report, for the first time, sub-4 nm mapping of donor:acceptor nanoparticle composition in eco-friendly colloidal dispersions for organic electronics. Low energy scanning transmission

electron microscopy (STEM) energy dispersive X-ray spectroscopy (EDX) mapping has revealed the internal morphology of organic semiconductor donor:acceptor blend nanoparticles at the sub-4 nm level. A unique element was available for utilisation as a fingerprint element to differentiate donor from acceptor material in each blend system. Si was used to map the location of donor polymer PTzBI-Si in PTzBI-Si:N2200 nanoparticles, and S (in addition to N) was used to map donor polymer TQ1 in TQ1:$PC_{71}BM$ nanoparticles. For select material blends, synchrotron-based scanning transmission X-ray microscopy (STXM), was demonstrated to remain as the superior chemical contrast technique for mapping organic donor:acceptor morphology, including for material combinations lacking a unique fingerprint element (e.g. PTQ10:Y6), or systems where the unique element is in a terminal functional group (unsaturated, dangling bonds) and can hence be easily damaged under the electron beam, e.g. F on PTQ10 donor polymer in the PTQ10:IDIC donor:acceptor blend. We provide both qualitative and quantitative compositional mapping of organic semiconductor nanoparticles with STEM EDX, with sub-domains resolved in nanoparticles as small as 30 nm in diameter. The sub-4 nm mapping technology reported here shows great promise for the optimisation of organic semiconductor blends for applications in organic electronics (solar cells and bioelectronics) and photocatalysis, and has further applications in organic core-shell nanomedicines.

TOC Graphic

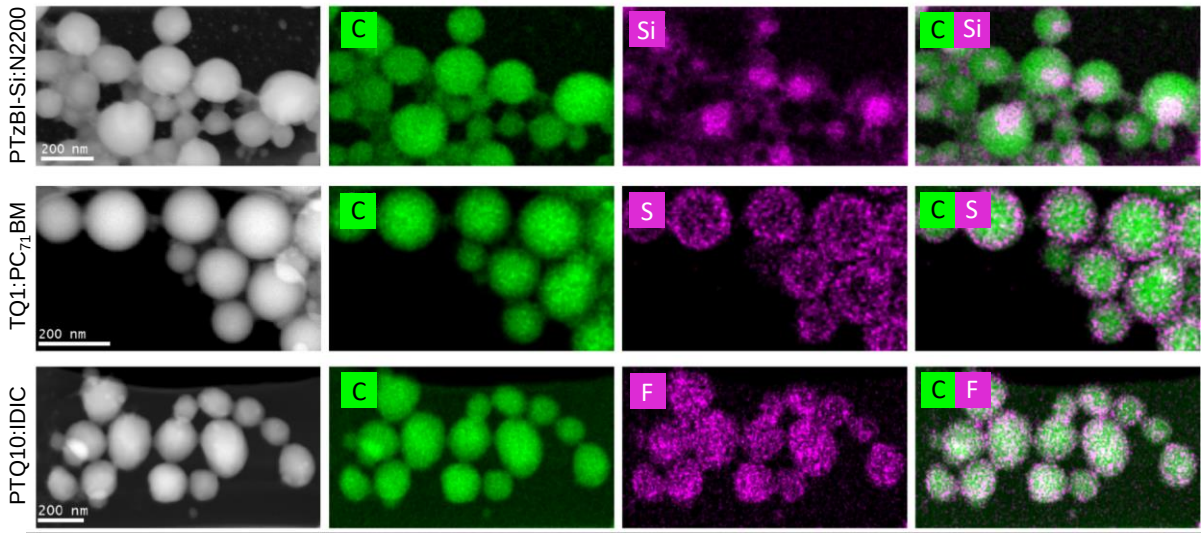

Introduction

While in silicon photovoltaics, light generates Mott-Wannier excitons which are dissociated at room temperature, in organic semiconductor materials Frenkel excitons are formed instead due

to their low dielectric constants. Hence, organic photovoltaic (OPV) devices require active layers made of molecular heterojunctions to split the excitons into free charges.[1,2] These molecular heterojunctions are comprised of a binary blend of electron donor and electron acceptor material, where the highest occupied molecular orbital (HOMO) and lowest unoccupied molecular orbital (LUMO) offsets are sufficient for exciton dissociation. Optimising the morphology of organic photovoltaic active layers comprising a donor-acceptor material blend has formed a significant focus area in this research field.[3] Particularly since the average diffusion length of an exciton is 10 nm,[4] and hence to reach efficient exciton dissociation rates, the active layer morphology must be engineered on the same length scale. Nanostructuring the donor-acceptor film morphology on the tens of nanometres length scale can be achieved by customising either solvent-cast bulk heterojunction (BHJ) films or water-coated nanoparticulate films.[5–10] The current power conversion efficiency (PCE) record of BHJ OPV is 19%.[11] Nanoparticulate-based OPV devices have improved significantly over recent years, with the current PCE record of 7.5%[8] holding potential for further improvement as new advances are made in understanding film morphology. The available morphology categories of nanoparticles include core-shell, Janus, and molecularly intermixed for two-component blends,[12] each with its own unique advantages for different applications. Interest in organic donor:acceptor semiconductor nanoparticles has also expanded to photocatalysis recently due to the work of Kosco et al.,[13] who reported increased photocatalytic activity and hydrogen evolution for colloidal nanoparticle systems. In this alternate application, the nanoparticles can be used in water-based colloidal form, meaning the additional fabrication step of coating the nanoparticles to form a thin solid film is not necessary.[14]

Non-fullerene acceptors (NFAs) have overtaken fullerene acceptors in organic photovoltaics and photocatalysis,[15–19] both BHJ and nanoparticulate, and the ability to map the morphology accurately is required for optimising structure-function relationships in device applications. In this report, we selected to study the new high performance donor-acceptor material systems PTzBI-Si:N2200 and PTQ10:IDIC, and the more well-known long-standing system TQ1:$PC_{71}BM$, a fullerene containing system. PTzBI-Si is a donor polymer based on a pyrrolo[3,4-f]benzotriazole-5,7(6*H*)-dione (TzBI) unit which was later functionalised with a siloxane side chain, increasing the PCE of OPV devices to 11% when combined with the polymeric NFA N2200.[20,21] All-polymer solar cell material pairs such as PTzBI-Si:N2200 are popular due to their high thermal, mechanical and photochemical stability and suitability to large area module production.[20] Molecular NFA IDIC (and it's structural analogue ITIC) has

shown promise as a low-bandgap n-type organic semiconductor in the past 5 years due to the advantages of easy tuning of electronic energy levels for its material sub-group, broad and strong light absorption, high electron mobility, and high morphological stability in comparison with fullerene derivative acceptors.[22,23] When combined with the newly developed donor polymer PTQ10, the maximum reported OPV PCE was 13%.[24] Wide bandgap polymer donor PTQ10 itself is a very promising organic semiconductor candidate for future energy applications due to its low-cost and simple synthesis via a two-step reaction, producing high yields (87%).[23] Sun et al.[23] reported the molecular design strategy of PTQ10 to be based on the donor–acceptor (D–A) copolymerisation concept, using a simple thiophene ring as donor unit in combination with a difluorine-substituted quinoxaline as acceptor unit.

It has long been a challenge to characterise donor-acceptor nanoparticle internal morphology due to the low contrast between organic semiconductors. Non-destructive techniques shown to provide contrast are STXM and cryo-TEM, but each have their own limitations. STXM is limited by its spatial resolution, and typically nanoparticles larger than 100 nm are analysed.[25–29] Cryo-TEM has high spatial resolution, sufficient for mapping domains within organic nanoparticles, but lacks chemical sensitivity. It is only suitable where one material is crystalline, which affords the use of regular lattice spacing for indication of domains of each material, as was demonstrated for the PTB7-Th:eh-IDTBR system by Kosco et al.[13] Energy-filtered TEM (EFTEM) and STEM energy-loss spectroscopy (EELS) mapping of organic donor:acceptor nanoparticles[30,31] and BHJ[32] films has, on the other hand, been reported. However, reports were each limited to a single polymer:fullerene material system, and a high spatial resolution for mapping the internal compositional structure of nanoparticles was not achieved. Most importantly, the destructive nature of high-energy TEM mapping of organics was not considered.[33] That includes acceleration voltages above 85 kV that is the C-C bond knock-on threshold, dose-rate dependent radiolysis damage and local electron beam heating up to 200 °C that is well above the glass-transition temperature (T_g) for the donor:acceptor nanoparticles.

In this work, we provide the first in-depth study of the STEM EDX mapping of organic semiconductor nanoparticle composition with sub-4 nm spatial resolution. We demonstrate non-destructive low-dose rate multi-frame averaged high S/N STEM EDX mapping at 60 kV.. These are conditions required to probe the length scales corresponding to the average exciton diffusion length in organic semiconductors, and without need of complex deconvolution methods used for ensemble averaged optical spectroscopy data. Three polymeric donors

(PTzBI-Si, TQ1 and PTQ10) were combined with three categories of acceptor materials, a polymeric NFA (N2200), a fullerene acceptor ($PC_{71}BM$) and a molecular NFA (IDIC) in the synthesis of binary blend nanoparticles using the miniemulsion route. The internal composition of the nanoparticles was also elucidated by synchrotron-based STXM – to provide a comparative technique that is widely accepted for studying organic semiconductor donor-acceptor material systems. We were able to demonstrate for the first time that the internal nanoscale structure can be resolved for particles in the size range optimal for OPV applications, 30 nm diameter. We demonstrate that this work expands the nanocharacterisation toolkit available for the analysis of nanoengineered colloids for a range of disciplines, including organic electronics, photocatalysis and nanomedicine.

Experimental

Materials

Poly{(4,8-bis(5-(2-ethylhexyl) thiophen-2-yl)benzo[1,2-b:4,5-b′]dithiophene-co-4,8-di(thien-2-yl)-2-(6-(1,1,1,3,5,5,5-heptamethyltrisiloxan-3-yl)hexyl)-6-octyl[1,2,3]triazolo[4,5-f]isoindole-5,7(2H,6H)-dione} (PTzBI-Si) ($(C_{71}H_{92}N_4O_4S_6Si_3)_n$) donor polymer was synthesised as described by Fan et al.[20] Poly [[6,7-difluoro[(2-hexyldecyl)oxy]-5,8-quinoxalinediyl]-2,5-thiophenediyl]] (PTQ10) ($(C_{28}H_{36}F_2N_2OS)_n$) donor polymer was purchased from Brilliant Matters (M_n 16,400 Da, Đ 3.01). Poly[2,3-bis-(3-octyloxyphenyl)quinoxaline-5,8-diyl-alt-thiophene-2,5-diyl] (TQ1) ($(C_{40}H_{46}N_2O_2S)_n$) donor polymer (M_n 53 100 Da, Đ 2.5) was synthesised by the copolymerisation of monomers 5,8-dibromo-6,7-difluoro-2,3-bis(3-(octyloxy)phenyl) quinoxaline and 2,5-bis-(trimethylstannanyl)thiophene, with the procedure described in detail elsewhere.[27,34] Poly{[N,N0-bis(2-octyldodecyl)naphthalene-1,4,5,8-bis(dicarboximide)-2,6-diyl]-alt-5,50-(2,20-bithiophene)} (N2200) ($(C_{62}H_{88}N_2O_4S_2)_n$) non-fullerene acceptor (also named PNDI-(2OD)2T) was purchased from 1-Material (M_n 55,000 Da, Đ 2.5). 2,2'-((2Z,2'Z)-((4,4,9,9-tetrahexyl-4,9-dihydro-s-indaceno[1,2-b:5,6-b']dithiophene-2,7-diyl)bis(methanylylidene)) bis(3-oxo-2,3-dihydro-1H-indene-2,1-diylidene)) dimalononitrile (IDIC) ($C_{66}H_{66}N_4O_2S_2$) non-fullerene acceptor was purchased from Ossila. (6,6)-Phenyl C_{71} butyric acid methyl ester ($PC_{71}BM$) ($C_{82}H_{14}O_2$) fullerene acceptor was synthesised according to Hummelen et al.[35] The chemical structures of the three polymer donor materials and three non-fullerene and fullerene acceptor materials are provided in Figure 1a. Sodium dodecyl sulfate (SDS) surfactant and chloroform solvent were purchased from Sigma-Aldrich.

Nanoparticle Synthesis

The miniemulsion organic phase (oil phase) was prepared by dissolving 15 mg of donor material (PTzBI-Si, PTQ10 or TQ1) and 15 mg of acceptor material (N2200, IDIC or $PC_{71}BM$) in 1.08 mL chloroform, forming a solution concentration of 27.8 $mg.mL^{-1}$. The miniemulsion aqueous phase was prepared by dissolving 0.5 mg of SDS surfactant in 2.8 mL of Milli-Q filtered water to form a solution concentration of 0.18 $mg.mL^{-1}$ for the PTzBI-Si:N2200 and PTQ10:IDIC miniemulsions, and by dissolving 1 mg of SDS surfactant in 2.8 mL of Milli-Q filtered water to form a solution concentration of 0.36 $mg.mL^{-1}$ for the TQ1:$PC_{71}BM$ miniemulsion. The surfactant concentration was purposely low so as to achieve a broad distribution in nanoparticle sizes for X-ray and EM mapping experiments. For subsequent nanoparticle synthesis for application in organic electronic devices it is recommended to use a higher surfactant concentration in order to achieve smaller sized nanoparticles, and additional dialysis steps to remove excess surfactant once the nanoparticles are formed, as reported in our previous work.[27] Macroemulsions were generated by combining the organic and aqueous phases and stirring at 1100 rpm, 33 °C for 1 h. A miniemulsion was generated using ultrasonication via a Hielscher UP400St ultrasonic processor with a 7 mm diameter tip. Sonication was at 30% amplitude, 27 W for 2 min, an ice bath was used to prevent overheating of the sample. Following sonication, the miniemulsion was transferred immediately to a hot plate for organic solvent evaporation at 60 °C with rapid stirring (1200 RPM). This evaporation was performed for a minimum of 3 h to ensure complete removal of organic solvent. The total volume of the nanoparticle colloidal dispersion was reduced to 0.5 mL via centrifugal dialysis with Amicon Ultra-4 10 kDa cut-off membrane centrifugal tubes and a Heraeus Biofuge Primo centrifuge, yielding nanoparticle dispersions with a solids content of 6 wt%.

Scanning Electron Microscopy

Samples were prepared for SEM by spin coating 2.5 μL of the nanoparticle colloidal dispersions (3000 rpm, 1 min, low acceleration of 112 $rpm.s^{-1}$) onto highly doped silicon substrates (Type N (phosphorus), resistivity 3–9 Ω.cm). The silicon substrates were UV-ozone cleaned for 10 min prior to spin coating. The nanoparticle films were sputter coated with 5 nm gold in a Safematic CCU-010 Compact Coating Unit prior to SEM measurements. SEM was performed on both a Zeiss Sigma VP HD FESEM and a Zeiss Auriga FIB-SEM (operating in SEM mode only), with an accelerating voltage of 3 kV, using the In Lens secondary electron detector.

Scanning Transmission Electron Microscopy

Low energy annular dark field (ADF) scanning transmission electron microscopy (STEM) was performed using a ThermoFisher (formerly FEI) double spherical aberration (Cs)-corrected Themis-Z 60-300, equipped with a high-brightness field emission (XFEG) gun operated at 60 kV. Chromatic aberrations were reduced by exciting a Wien-type monochromator to +0.6 V. Low dose imaging (< 10 pA) was controlled by the monochromator defocus. Spherical aberrations were corrected using a CEOS DCOR+ corrector achieving a resolution of <1.0 Ångström. The convergence angle was set to 17.9 mrad and a collection range of 45-160 mrad was employed using a high angle annular dark field (HAADF) detector. A Super-X energy dispersive X-ray spectroscopy (EDS) detector was used at a 0.2 - 20 keV energy range to acquire EDX maps and the Velox software was employed to perform EDX quantification with Brown-Powell ionisation cross-section models and using built-in routines for multiple frame noise reduction. Low dose-rate multiple scan raster imaging was carried out at 0.1 $e^-/Å^2$ (0.5 pA current, pixel size 8.9 Å) using 2 µs dwell time. The total counts of all EDX maps was between 10^6 and 10^7.

TEM samples were prepared by vertical immersion of lacey carbon on Cu mesh support grids in the colloidal suspension followed by drying excessive suspension on grade 292 filter paper. The samples were subsequently dried at 10^{-5} mbar pressure at room temperature for 10 min. prior to insertion in the TEM.

Correlative Transmission Electron Microscopy

Correlative TEM was used post-STXM to reimage the same nanoparticles for collecting position-matched micrographs. The Si_3N_4 membrane substrates with deposited nanoparticles were transported back to the University of Sydney (Australia) to measure TEM on a JEOL JEM-1400 at an accelerating voltage of 120 kV, using a Norcada custom TEM holder for Si_3N_4 membrane substrates (NTS-J-NX5-001).

Synchrotron NEXAFS Spectroscopy

NEXAFS at the C K-edge was utilised for the measurement of organic semiconductors in this study. Measurements of PTzBI-Si, PTQ10 and TQ1 donor polymers and N2200, IDIC and $PC_{71}BM$ non-fullerene and fullerene acceptors were performed at two synchrotron beamlines, the PolLux beamline (X07DA) at the Swiss Light Source (SLS) (Villigen, Switzerland) and the Polymer STXM 5.3.2.2 beamline of the Advanced Light Source (ALS) (Berkeley, USA).

Pristine films of each organic semiconductor material were prepared by spin coating chloroform or chlorobenzene solutions of each material onto PEDOT:PSS (AI 4083 purchased from Ossila) coated glass substrates. 2 x 2 mm^2 sections were scored on the films using a scalpel, followed by floating off the film sections onto a D.I. water surface, which was made possible by dissolving the PEDOT:PSS sacrificial layer under the semiconductor material films (for floating off method refer to He et al.[36]). 2 x 2 mm^2 film sections were subsequently collected onto 300 mesh Cu grids (20 mm bar, 63 mm hole, 3 mm diameter, purchased from ProSciTech Pty Ltd) for NEXAFS measurements. NEXAFS linescans were performed for each pristine material film, and the energy of the X-ray beam was varied between 278 and 390 eV, spanning the C K-edge region. Second- and third-order light was removed, at the SLS, by an order sorting aperture and higher order suppressor (further details are provided in Frommherz et al.[37]), and at the ALS by an order sorting aperture and an N_2 gas filter (further details are provided in Kilcoyne et al.[38]). Orthogonal energies for later STXM mapping were selected by overlaying NEXAFS spectra of each donor:acceptor material combination, PTzBI-Si:N2200, PTQ10:IDIC and TQ1:$PC_{71}BM$.

Synchrotron X-ray Spectromicroscopy

X-ray spectromicroscopy (scanning transmission X-ray microscopy, STXM) measurements were performed at two synchrotron beamlines, the PolLux[39,40] beamline (X07DA) at the Swiss Light Source and the Polymer STXM 5.3.2.2 beamline of the Advanced Light Source. Samples were prepared for STXM measurements by spin coating 2.5 μL of nanoparticle dispersions onto low stress silicon nitride (Si_3N_4) membrane windows (window dimensions 1 x 1 mm^2, window thickness 30 nm, silicon frame dimensions 5 x 5 mm^2, purchased from Silson, UK) at 3000 rpm, 1 min, low acceleration. Samples were air dried at room temperature. The samples on Si_3N_4 windows were loaded in the STXM sample chamber and rastered with respect to the X-ray beam. The transmitted X-ray beam is detected by a scintillator and a photomultiplier tube. The STXM Fresnel zone plate (Ni at SLS, Au at ALS) had an outer most zone width of 25 nm, setting the spatial resolution limit of the measurement. The transmitted X-ray beam is detected by a scintillator and a photomultiplier tube.[38] Singular value decomposition (SVD) was used to fit a sum of the pristine material NEXAFS spectra to the measured blend spectrum of the nanoparticles, at each pixel, in the STXM images. Prior to SVD fitting, the pristine material NEXAFS spectra were normalised to film thickness. The method of reference-spectrum normalisation constitutes dividing the real spectrum by a theoretical spectrum calculated based on the material's chemical formula using

henke.lbl.gov/optical_constants/filter.html. The aXis2000 package (unicorn.mcmaster.ca/aXis2000.html) was used to perform image analysis of STXM maps. Further details of STXM experimental methods and data analysis methods can be found in the literature.[41]

UV-Visible and Photoluminescence Spectroscopy

UV-visible spectra were recorded using a SAFAS UV mc² spectrophotometer in double beam mode. Spectra were recorded from 200 to 1000 nm in steps of 2 nm and using an integration time of 1s. Quartz cuvettes with 1 cm optical path were used. Steady-state photoluminescence (PL) spectra were recorded using a PTI (Photon Technology International) Quantmaster 40 setup with a Xenon arc lamp coupled with two monochromators: one for excitation and one for the emission. The detection system is based on a photomultiplier (Model 810/814). The excitation wavelength (λ_{exc}) was set at 566 nm for PTzBI-Si:N2200 and PTQ10:IDIC, and 600 nm for TQ1:$PC_{71}BM$. The emission spectra was recorded with 1 nm step and using an integration time of 1s, from 600 to 900 nm for PTzBI-Si:N2200 and PTQ10:IDIC, and from 650 to 875 nm for TQ1:$PC_{71}BM$. The excitation and emission slits were all set at 1.5 mm corresponding to a spectral resolution of 6 nm. 4-sided quartz cuvettes with 1 cm optical path were used for these PL experiments. The different dispersions were diluted with water to reach an optical density of 0.25 at the excitation wavelength.

Results and Discussion

Nanomaterials Synthesis

Two component nanoparticles were synthesised via the miniemulsion method[42] for the donor–acceptor material systems PTzBI-Si:N2200, TQ1:$PC_{71}BM$ and PTQ10:IDIC. A 1 : 1 w/w ratio was applied to all systems, with a summary of the material properties of the organic semiconductors provided in Table 1 and the nanoparticle synthesis parameters in Table 2. The internal morphology of PTzBI-Si:N2200 and PTQ10:IDIC nanoparticles has not previously been reported, whereas for TQ1:$PC_{71}BM$ nanoparticles we have previously reported the internal morphology of 1:3 w/w ratio donor:acceptor nanoparticles to be core-shell, with a TQ1-rich shell and $PC_{71}BM$-rich core.[27] The particle size and size distribution for each nanoparticle sample is provided in Figure 1e-g and tabulated in Table 2, with the mean value used as an indicator of nanoparticle size and the standard deviation (σ) used as an indicator of the size distribution. The nanoparticle size was measured by applying a circular Hough transform algorithm to SEM images of nanoparticle films (Figure 1b-d) in MATLAB, with

further method details provided elsewhere.[27] This method gave diameters of 113 ± 42 nm for the PTzBI-Si:N2200 nanoparticles; 144 ± 56 nm for the TQ1:$PC_{71}BM$ nanoparticles and 120 ± 53 nm for the PTQ10:IDIC nanoparticles. Further particle size analysis was performed on high magnification STEM images to account for nanoparticles of diameter <50 nm which are traditionally not captured in large area SEM survey scan analysis. These additional size distribution plots are provided in Supplementary Material Figure S7.

Table 1. Material properties of the organic semiconductors.

Material	Classification	Chemical Formula	Unique Mapping Element	E_g (eV)
Donor				
PTzBI-Si	Polymer	$(C_{71}H_{92}N_4O_4S_6Si_3)_n$	Si	1.78
TQ1	Polymer	$(C_{40}H_{46}N_2O_2S)_n$	S, N	1.7
PTQ10	Polymer	$(C_{28}H_{36}F_2N_2OS)_n$	F	1.95
Non-fullerene acceptor				
N2200	Polymer	$(C_{62}H_{88}N_2O_4S_2)_n$	-	1.44
IDIC	Small Molecule	$C_{66}H_{66}N_4O_2S_2$	-	1.62
Fullerene acceptor				
$PC_{71}BM$	Small Molecule	$C_{82}H_{14}O_2$	-	2.2

Table 2. Concentration of the initial organic phase (C_{org}) and surfactant-containing aqueous phase (C_{aq}) for the miniemulsion synthesis of donor:acceptor nanoparticles. Nanoparticle size and size distribution (σ), calculated using circular Hough transform analysis of SEM images (number of nanoparticles, n, sampled is listed).

Donor: Acceptor System	Donor: Acceptor Ratio	C_{org} (mg.mL^{-1})	C_{aq} (mg.mL^{-1})	Nanoparticle Diameter (nm)			
				Mean	σ	Median	n
PTzBI-Si:N2200	1:1	27.8	0.18	113	42	107	1109
TQ1:$PC_{71}BM$	1:1	27.8	0.36	144	56	138	744
PTQ10:IDIC	1:1	27.8	0.18	120	53	112	1223

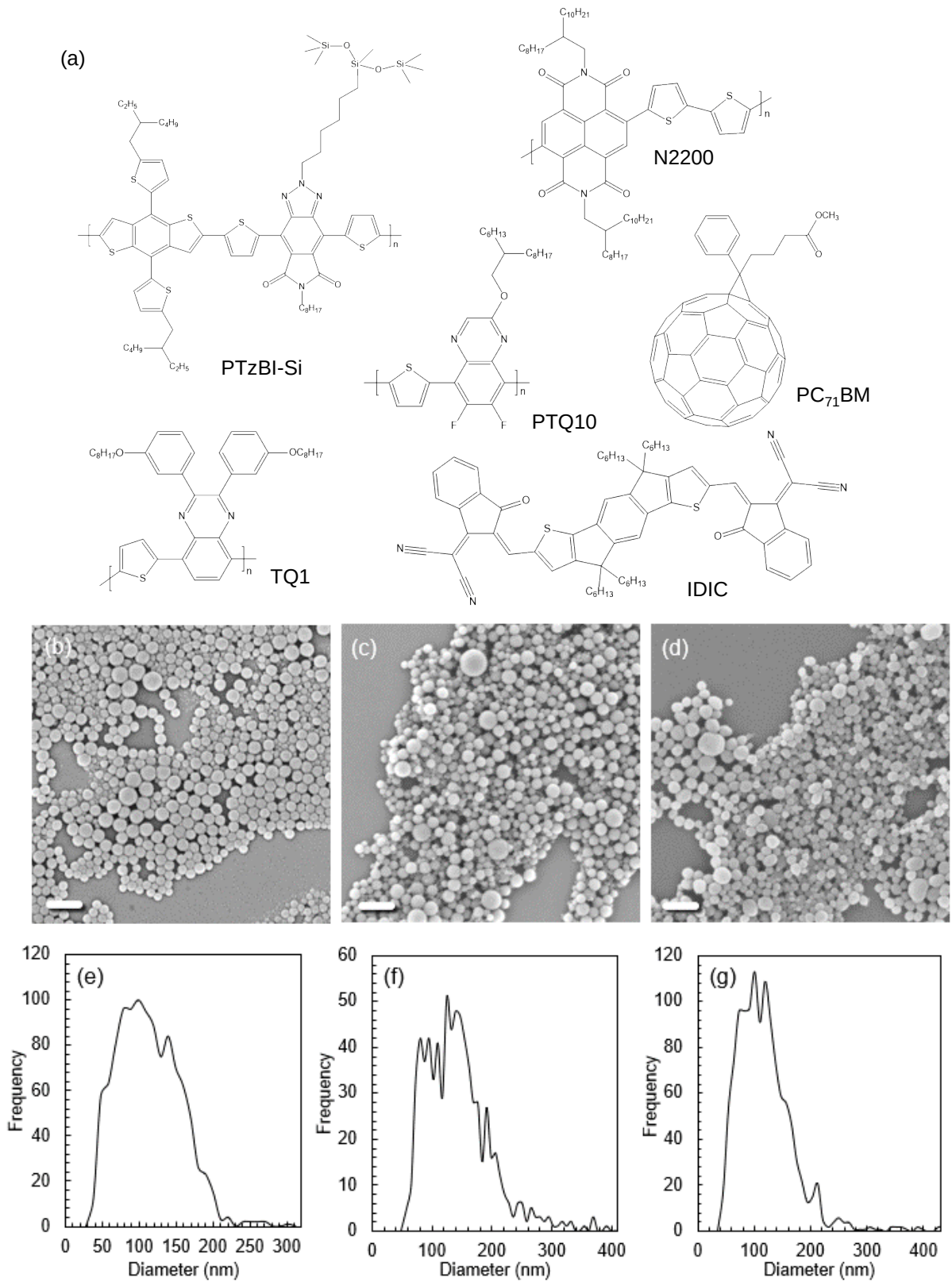

Figure 1. (a) Chemical structure of organic semiconductors PTzBI-Si, PTQ10, TQ1, N2200, IDIC, $PC_{71}BM$. (b-d) SEM and (e-g) particle size distribution plots showing the shape and size distribution of (b, e) PTzBI-Si:N2200 nanoparticles, (c, f) TQ1:$PC_{71}BM$ nanoparticles and (d, g) PTQ10:IDIC nanoparticles. Scale bars are 500 nm.

Sub-4 nm Mapping of Nanoparticle Structure – Unique Element Mapping

The three donor–acceptor material systems each possess a unique element that was able to be utilised as a fingerprint element to differentiate donor from acceptor material when mapping the internal nanoparticle morphology. Si is present in donor polymer PTzBI-Si and absent from NFA N2200, hence useful for the PTzBI-Si:N2200 system; S (in addition to N) is unique to donor polymer TQ1 and absent from $PC_{71}BM$ in the TQ1:$PC_{71}BM$ system; and F is unique to PTQ10 donor polymer and absent from IDIC in the PTQ10:IDIC system.

Low energy STEM EDX mapping is a powerful technique to elucidate composition of organic core-shell nanoparticles. At 60 kV operation voltage, the knock-on damage threshold is well below the C-C bond energy, leaving radiolysis and electron beam induced heating the main damage mechanisms.[43] By further controlling the dose-rate of a multiple scan raster image the radiolysis and beam-heating can be significantly reduced while keeping a high S/N.[44] Dose-rate limits were previously reported for P3HT and $PC_{61}BM$, for example.[45] 0.1 $e^-/Å^2$ was reported for $PC_{61}BM$. For that reason, the total electron dose per pixel for each scan was set to 0.1 $e^-/Å^2$ for the high-resolution STEM EDX maps (0.5 pA current, 2 µs dwell time, pixel size 8.9 Å). The increased ionisation scattering cross-section at 60 kV further increases the EDX signal yield at 60 kV (as compared to at 200 or 300 kV), rendering STEM EDX a viable option for organic material as long as a low-dose rate raster imaging is maintained.[46] STEM EDX typically has a lower resolution compared to STEM imaging. This is largely an effect of delocalisation stemming from the convolution of the probe with the larger ionisation cross-section (Brown-Powel) of atomic orbitals that accounts for EDX contrast, compared to the Rutherford and thermal diffuse scattering cross-section that describes electron-nuclei scattering in STEM contrast. The delocalisation of STEM EDX can be estimated by measuring the width of the rising slope at atomically sharp compositional interfaces in STEM EDX maps. The spatial resolution of the STEM together with STEM EDX maps (see Supplementary Material Figure S6), yields sub-nanometre mapping precision, which is highly suitable for mapping the composition of organic semiconductor nanoparticle morphology and a substantial improvement on the spatial resolution of comparative techniques such as synchrotron-based STXM.

Figure 2 shows STEM EDX maps of PTzBI-Si:N2200 1:1 donor:acceptor blend nanoparticles. In (a) the ADF image demonstrates an asymmetric distribution of mass and particles exhibit an elliptical appearance. Figure 2(b-f) show the elemental maps of (b) S-K (teal-blue), (c) O-K

(yellow), (d) C-K (green), (e) Si-K (purple) and (f) overlay of C (green) and Si (purple), respectively. Additional nanoparticles of PTzBI-Si:N2200 were mapped (at the same K-edge energies) and the elemental maps are provided in Supplementary Material Figure S1. The EDX spectrum is provided in Figure S5a, the peaks assigned comprised S-K at 2.31 keV, O-K at 0.52 keV, C-K at 0.27 keV, and Si-K at 1.74 keV. Si located in a siloxane functional group is unique to PTzBI-Si donor polymer (Figure 1a) and occupies the off-centred core of these Janus nanoparticles, as evidenced by the location of Si at the nanoparticle centre in Figure 2e, and the C+Si map overlay in Figure 2f. It is furthermore observed that the off-centred core has a higher concentration of S compared to the shell, as expected considering in PTzBI-Si the ratio of S to C (1:12) is three times higher than that of S to C (1:31) in N2200. The Janus morphology for the PTzBI-Si:N2200 nanoparticle system measured via STEM EDX is supported by synchrotron-based STXM mapping (Figure 5a-d), where the same morphology is observed. Compositional analysis of the STEM EDX maps shows a 72 (± 7) % N2200 composition in the nanoparticle shell and a 94 (± 2) % PTzBI-Si composition in the nanoparticle off-centred core.

A core-shell morphology is the most commonly reported morphology category for nanoparticles synthesised via the miniemulsion method. The core-shell structure formation via self-assembly based on the surface energy differential of donor and acceptor material is a phenomenon reported in our previous work for a range of donor-acceptor material systems.[29] During nanoparticle formation, to lower the energy of the free surface the lower surface energy material of the two materials is driven to the nanoparticle shell, and the higher surface energy material is driven to the nanoparticle core. PTzBI-Si is a new organic semiconductor with a surface energy yet to be reported. Our previous studies of donor:acceptor nanoparticles incorporating the low surface energy NFA N2200 (23.7 $mJ.m^{-2}$),[47] namely P3HT:N2200 and TQ1:N2200,[29] have similarly demonstrated an off-centred polymer core and N2200-rich shell nanoparticle morphology, approaching Janus.

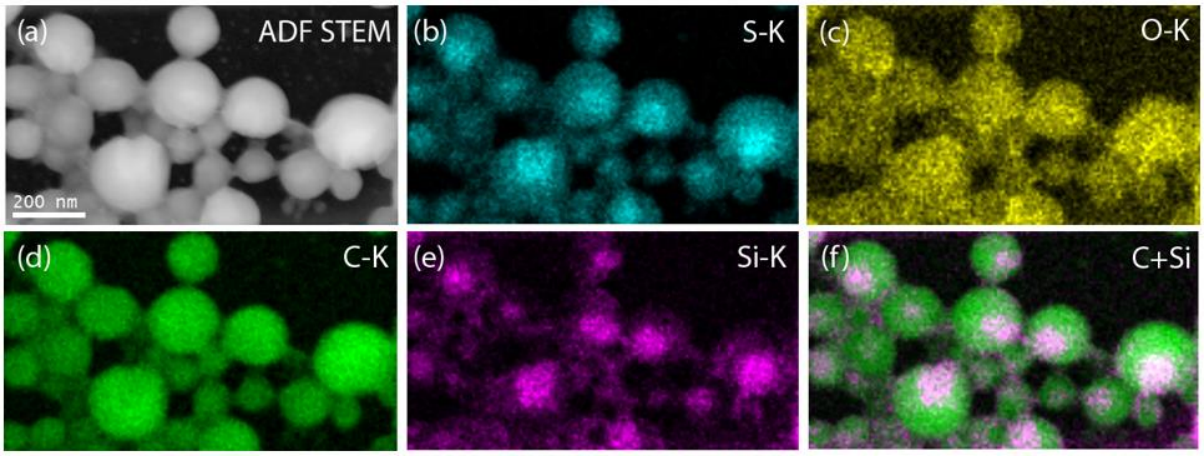

Figure 2. (a) ADF image and (b-f) STEM-EDX K-edge maps of 1:1 PTzBI-Si:N2200 nanoparticles showing Si (purple) unique to PTzBI-Si donor polymer (and S (blue) at higher loading in the donor polymer) located at a higher concentration at the nanoparticle centre. In order (b) S-K (blue), (c) O-K (yellow), (d) C-K (green), (e) Si-K (purple) and (f) overlay of C (green) and Si (purple). Scale bars are 200 nm.

STEM EDX maps of the 1:1 TQ1:$PC_{71}BM$ nanoparticles are presented in Figure 3. In contrast to PTzBI-Si:N2200, TQ1:$PC_{71}BM$ nanoparticles are spherically shaped and a core-shell structure is clearly visible by mass contrast, as evidenced in the high resolution ADF image in Supplementary Material Figure S3. The EDX maps in (b-f), showing (b) N-K (teal-blue), (c) O-K (yellow), (d) C-K (green), (e) S-K (purple) and (f) overlay of C (green) and S (purple), respectively. Additional nanoparticles of TQ1:$PC_{71}BM$ were mapped (at the same K-edge energies) and the elemental maps are provided in Supplementary Material Figure S2. The EDX spectrum is provided in Figure S5b, the peaks assigned comprised N-K at 0.39 keV, O-K at 0.52 keV, C-K at 0.27 keV, and S-K at 2.32 keV. N in the quinoxaline unit and S in the thiophene unit are unique to the TQ1 donor polymer (Figure 1a) which occupies the shell of the core-shell nanoparticles, as clearly observed by the location of S in Figure 3e, N in Figure 3b, and the C+S map overlay in Figure 3f. Compositional analysis of the STEM EDX maps of TQ1:$PC_{71}BM$ nanoparticles shows a 71 (± 14) % TQ1 composition in the nanoparticle shell and an 81 (± 3) % $PC_{71}BM$ composition in the nanoparticle core.

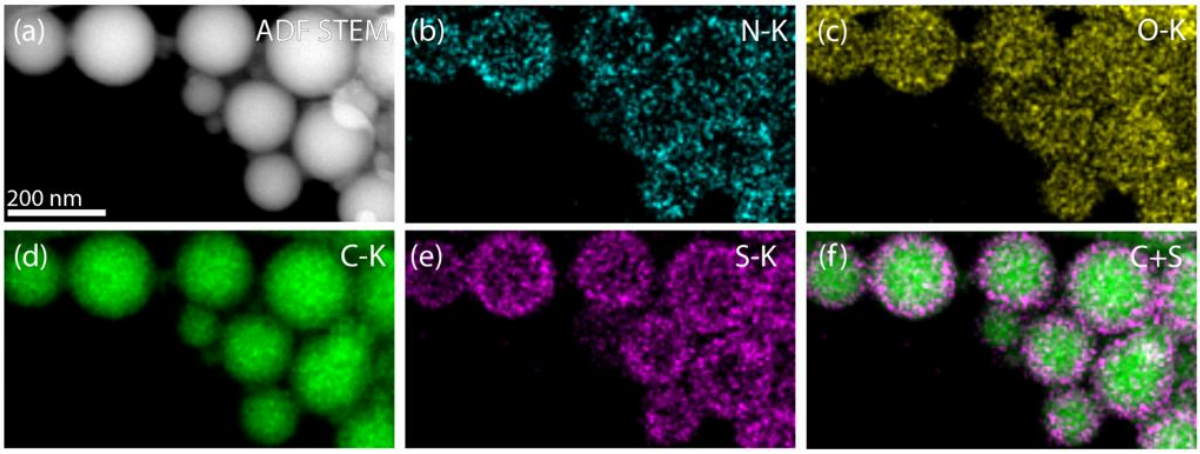

Figure 3. (a) ADF image and (b-f) STEM-EDX K-edge maps of 1:1 TQ1:$PC_{71}BM$ nanoparticles showing N (blue) and S (purple) unique to TQ1 donor polymer located at a higher concentration at the nanoparticle shell. In order (b) N-K (blue), (c) O-K (yellow), (d) C-K (green), (e) S-K (purple) and (f) overlay of C (green) and S (purple). Scale bars are 200 nm.

In Figure 4, a 1:1 PTQ10:IDIC nanoparticle blend is presented. Figure 4a shows the ADF image that indicates an elliptical shape of the particles. The ADF mass contrast imaging mode further suggests a uniform distribution of elements as opposed to a core-shell structure. Figure 4 (b-f) show STEM EDX maps of (b) S-K (blue), (c) O-K (yellow), (d) C-K (green), (e) F-K (purple) and (f) overlay of C (green) and F (purple), respectively. In particular, F-K maps show a uniform distribution within the particle. This result is in contradiction with STXM mapping which shows that the PTQ10 donor polymer occupies the shell of the core-shell nanoparticles (Figure 5(i-l)). It is possible that the unsaturated F-terminations on the quinoxaline units in PTQ10 (Figure 1a) diffuse into the nanoparticles because of electron beam interaction causing atom displacement, rendering F-mapping inaccurate. The C-F bond in PTQ10 is 1.41 Å, corresponding to a bond dissociation energy of 3.5 eV.[48] That is on the same order as the electron-nuclei energy transfer at 60 kV for a low atomic mass element such as F,[49] and arguably the reason for the lack of a higher measured concentration of F in the shell. Additional nanoparticles of PTQ10:IDIC were mapped (at the same K-edge energies) and the elemental maps are provided in Supplementary Material Figure S4. The EDX spectrum is provided in Figure S5c, the peaks assigned comprised S-K at 2.31 keV, O-K at 0.53 keV, C-K at 0.27 keV, and F-K at 0.68 keV.

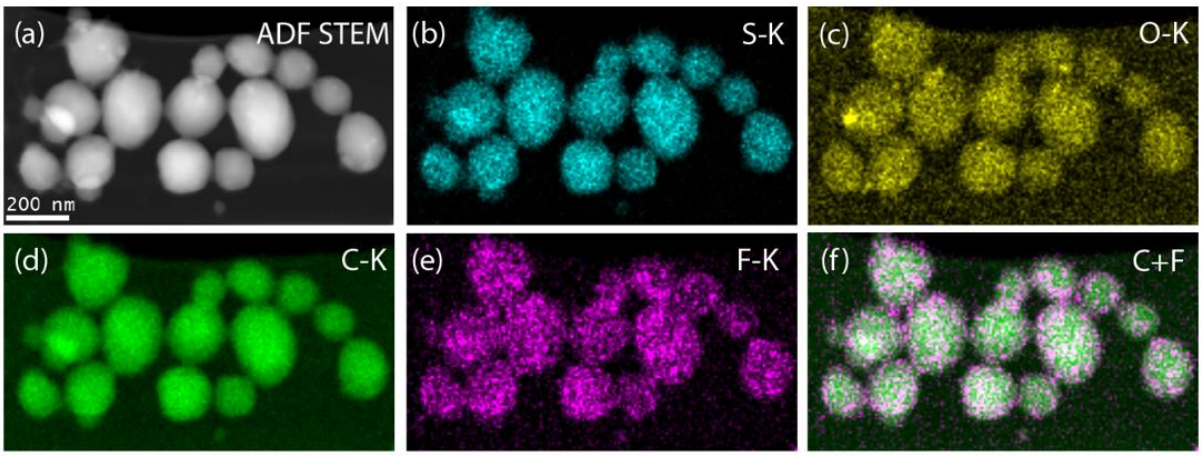

Figure 4. (a) ADF image and (b-f) STEM-EDX K-edge maps of 1:1 PTQ10:IDIC nanoparticles showing F (purple) unique to PTQ10 donor polymer. In order (b) S-K (blue), (c) O-K (yellow), (d) C-K (green), (e) F-K (purple) and (f) overlay of C (green) and F (purple). Scale bars are 200 nm.

PTQ10:IDIC is not the only material system where deferring to synchrotron-based STXM mapping is still beneficial. Donor:acceptor material systems that do not possess a unique fingerprint element for mapping will also need to rely on long-standing techniques such as STXM for mapping composition. Such systems include PTQ10:Y6 (with a record PCE of 16%)[24], where the chemical structure of narrow bandgap NFA Y6 ($C_{82}H_{86}F_4N_8O_2S_5$) contains the same elements as the wide bandgap polymer donor PTQ10 ($(C_{28}H_{36}F_2N_2OS)_n$), hence providing no unique elements for STEM EDX mapping capacity.

Synchrotron X-ray Mapping of Nanostructure

Unlike STEM EDX, synchrotron-based STXM is not based on unique elemental analysis, it is based on relative absorption in the soft X-ray energy range. NEXAFS provides a fingerprint spectrum that is unique to each component of a blend system by probing the element-specific excitations of core electrons to unoccupied molecular orbitals.[50] NEXAFS and STXM measurements were performed using beamline 5.3.2.2 at the ALS synchrotron and the PolLux beamline (X07DA) at the SLS synchrotron to ascertain the internal nanostructure of the donor–acceptor nanoparticles. The resolution limit of STXM is typically 30 nm, set by the outermost zone width of the Fresnel zone plate utilised for focusing the incoming X-ray beam. This spatial resolution limit for STXM is an order of magnitude larger than that of STEM EDX, highlighting the benefit of STEM EDX, where applicable. For further information on STEM EDX compared to STXM as a nanoscale mapping technique with chemical contrast, we refer the reader to Table S1 (Supplementary Material).

Figure S8 presents the NEXAFS spectra of PTzBI-Si, TQ1 and PTQ10 donor polymers and N2200, $PC_{71}BM$ and IDIC non-fullerene and fullerene acceptors. STXM was utilised to collect X-ray maps of nanoparticle films at multiple photon energies of the incident beam, representing orthogonal energies selected from overlaying pristine film NEXAFS spectra. Singular value decomposition (SVD) was employed to determine the relative ratio of donor and acceptor component (at each pixel) in the composite nanoparticles. STXM composition maps are presented in Figure 5 for PTzBI-Si:N2200 (a-d), TQ1:$PC_{71}BM$ (e-h) and PTQ10:IDIC (i-l) nanoparticles. Additional nanoparticles of PTzBI-Si:N2200, TQ1:$PC_{71}BM$ and PTQ10:IDIC were analysed and the STXM maps are provided in Supplementary Material Figure S9, S10 and S11, respectively. A Janus morphology is observed for the PTzBI-Si:N2200 systems and a core–shell structure for the TQ1:$PC_{71}BM$ and PTQ10:IDIC systems, with varying composition of individual domains depending on the donor–acceptor material combination. For the PTzBI-Si:N2200 nanoparticle system characterised via STXM, a PTzBI-Si-rich off-centred core and N2200-rich shell was measured, as depicted in Figure 5(a–d). For the TQ1:$PC_{71}BM$ nanoparticles, the structure inverted to donor-rich shell (a TQ1-rich shell) and an acceptor-rich core (a $PC_{71}BM$-rich core), as depicted in Figure 5(e-h). A TQ1-rich shell is evident by the bright rings observed in the TQ1 STXM fractional composition map for the 1 : 1 nanoparticles (Figure 5e). Thirdly, for the PTQ10:IDIC nanoparticle system, a PTQ10-rich shell and IDIC-rich core was measured via STXM mapping (Figure 5(i-l)), although the domain purity of the shell is lower indicating that this domain potentially tends towards a molecularly mixed state. We know from our previous work that the core-shell morphology forms via self-assembly of materials in accordance with their relative surface energies.[29] The donor and acceptor materials self-arrange in the miniemulsion droplets (swollen micelles) to minimise surface energy, while the oil-phase solvent (e.g. chloroform or o-xylene[51]) is being removed via thermal evaporation.

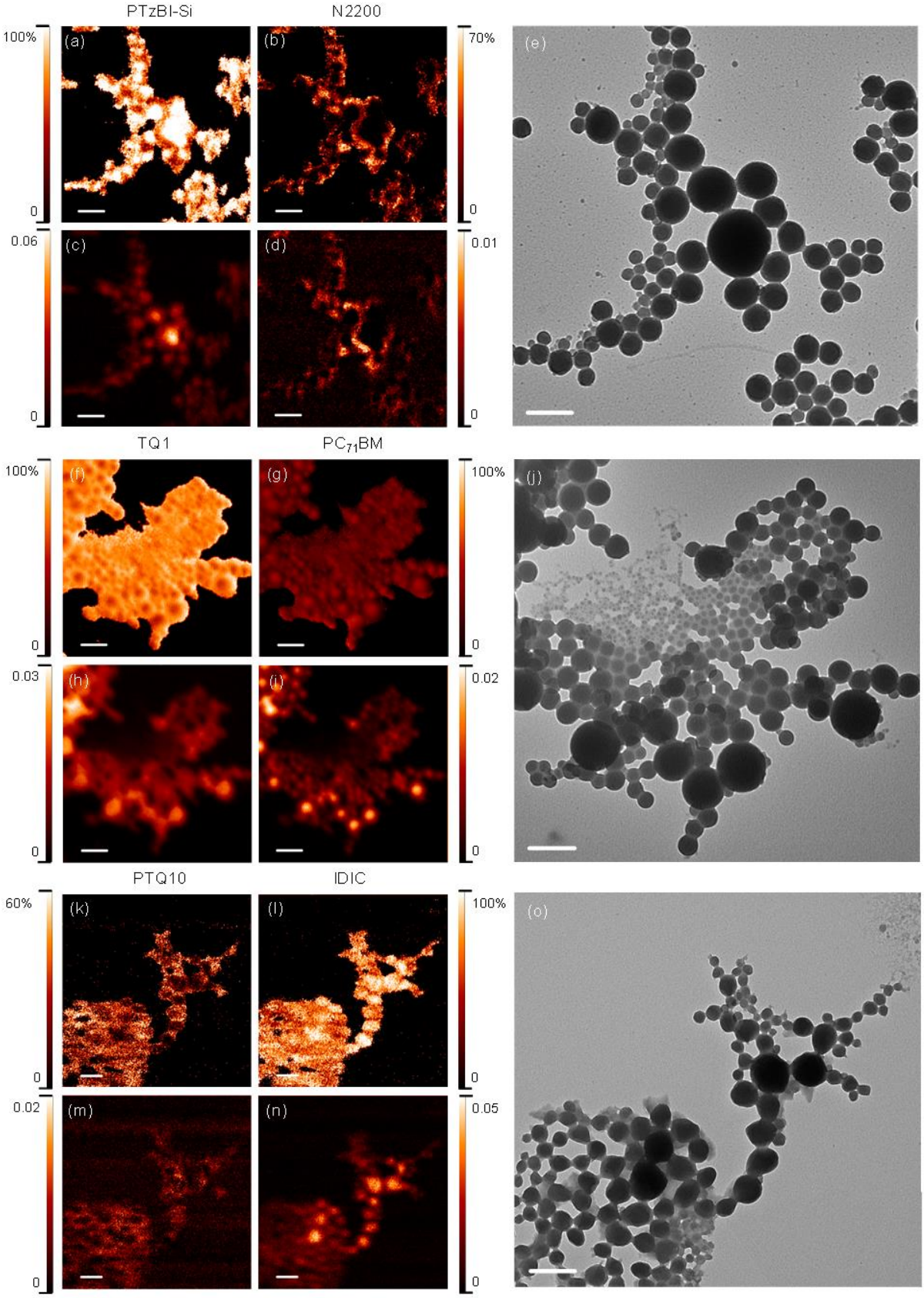

Figure 5. STXM fractional composition maps showing the concentration of (a) PTzBI-Si and (b) N2200 with corresponding STXM mass plots (c and d) and (e) correlative TEM for 1:1 PTzBI-Si : N2200 nanoparticles. STXM fractional composition maps showing the concentration of (f) TQ1 and (g) $PC_{71}BM$ with corresponding STXM mass plots (h and i) and (j) correlative TEM for 1:1 TQ1 : $PC_{71}BM$

nanoparticles. STXM fractional composition maps showing the concentration of (k) PTQ10 and (l) IDIC with corresponding STXM mass plots (m and n) and (o) correlative TEM for 1:1 PTQ10 : IDIC nanoparticles. All scale bars are 500 nm. The colour contrast is scaled such that light colours correspond to higher component concentrations. For the mass plots (c, d, g, h, k, l) the colour scale bars indicate concentration of component in mg.cm^{-2}.

Relevance of Sub-4 nm Length Scales

With STEM-EDX mapping we were able to resolve the composition of core-shell nanoparticles as small as 30 nm in diameter (Figure 6). With 25–30 nm being the average size of nanoparticles used in nanoparticle OPV applications,[25,27,51,52] we highlight that this higher spatial resolution technique has benefits for the OPV research field. In Figure 6 we present STEM EDX maps of a range of nanoparticle sizes for the TQ1:$PC_{71}BM$ nanoparticle system (30 to 350 nm diameter), showing the smallest nanoparticles that can have their internal morphology reliably mapped.

STXM has previously been used to measure the internal morphology of organic semiconductor nanoparticles of diameter 100–400 nm, a larger size than that used in nanoparticle OPV applications. The reason for this disparity in nanoparticle size measured with STXM and nanoparticle size applied to OPV device fabrication was the inability to resolve the internal structure of nanoparticles smaller than 100 nm, due to the resolution limit of the STXM technique. Hence STXM studies usually measured the morphology over a range of sizes (100–400 nm) and extrapolated to smaller sizes, claiming that the morphology of 25–30 nm nanoparticles would be consistent. Herein, we can now report that this assumption is correct; the morphology of smaller device-appropriate nanoparticles is indeed consistent, with the same core-shell morphology observed for nanoparticles over the full size range in this study, 30–350 nm (Figure 6).

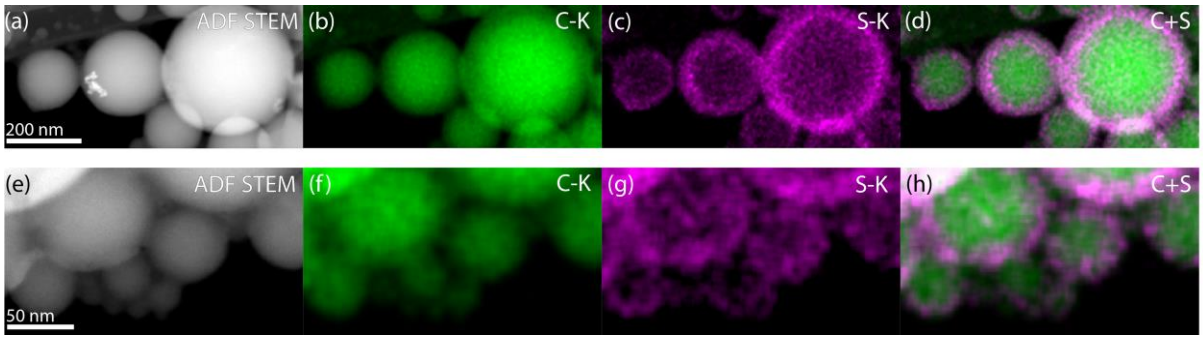

Figure 6. STEM-EDX K-edge maps demonstrating the smallest feature size that can be measured. (a-d) Mapping of 1:1 TQ1:$PC_{71}BM$ nanoparticles of diameter 150 to 350 nm, and (e-h) of diameter 30 to 100 nm. In order (a, e) HAADF, (b, f) C (green), (c, g) S (purple), (d, h) overlay of C (green) and S (purple).

Quantitative Analysis of Donor-Acceptor Nanoparticles

The composition of nanoparticles was quantified on the single-particle level with STEM EDX for the PTzBI-Si:N2200 and TQ1:$PC_{71}BM$ material systems and with synchrotron-based STXM for the PTQ10:IDIC material system. Considering the PTzBI-Si:N2200 nanoparticles possessed a Janus structure, line profiles as opposed to radial profiles were used to measure the composition of domains. Table 3 shows the average composition data acquired from 9, 7 and 10 nanoparticles of the PTzBI-Si:N2200, TQ1:$PC_{71}BM$ and PTQ10:IDIC systems, respectively. The differing sample size for STEM EDX data stems from exclusion of particles overlapping with the C background from the TEM grid and from adjacent particles. The core and shell compositions for PTQ10:IDIC nanoparticles in Table 3 were calculated (in MATLAB) from radial profiles of nanoparticles using the core-shell model reported by Holmes et al.[26] On average, the PTzBI-SI:N2200 nanoparticles are comprised of a 72 (± 7) % N2200 shell and a 94 (± 2) % off-centred PTzBI-Si core; the TQ1:$PC_{71}BM$ nanoparticles are comprised of a 71 (± 14) % TQ1 shell and an 81 (± 3) % $PC_{71}BM$ core; and the PTQ10:IDIC nanoparticles are comprised of a 62 (± 9) % PTQ10 shell and a 76 (± 4) % IDIC core. A characteristic line profile of a PTzBI-Si:N2200 nanoparticle in two size bins is presented in Figure 7a,d, and an average profile in Figure 7g. Radial profiles were generated for TQ1:$PC_{71}BM$ and PTQ10:IDIC nanoparticles, which were more symmetrical and uniform in nature. A characteristic radial profile of a TQ1:$PC_{71}BM$ nanoparticle in two size bins is presented in Figure 7b,e, and a PTQ10:IDIC nanoparticle in two size bins is presented in Figure 7c,f. An average radial profile for these two systems in presented in Figure 7h and i. We observed a small broadening of the donor-acceptor domain interface as nanoparticle size decreased, for all nanoparticle types. The relationship between nanoparticle shell thickness and particle diameter is plotted in Supplementary Material Figure S12. The results show that as nanoparticle diameter increases, shell thickness increases for both PTzBI-Si:N2200 and TQ1:$PC_{71}BM$ nanoparticles, whereas for PTQ10:IDIC nanoparticles the shell thickness on average remains the same.

Table 3. Average compositional analysis of donor–acceptor nanoparticles, as calculated from STEM EDX (for PTzBI-Si:N2200 and TQ1:$PC_{71}BM$ nanoparticles) and STXM maps (for PTQ10:IDIC nanoparticles). Abbreviations are as follows: NP_S (nanoparticle shell), OS_S (predominant organic semiconductor comprising the shell), NP_C (nanoparticle core), OS_C (predominant organic semiconductor comprising the core).

Donor: Acceptor System	**Morphology classification**	**NP_S**		**NP_C**	
		OS_S	**Composition (%) (σ)**	**OS_C**	**Composition (%) (σ)**
STEM EDX analysis outputs					
PTzBI-Si: N2200	Janus (Off-centred core)	N2200	PTzBI-Si: 28 (7) N2200: 72 (7)	PTzBI-Si	PTzBI-Si: 94 (2) N2200: 6 (2)
TQ1:$PC_{71}BM$	Core-shell with high donor-acceptor intermixing	TQ1	TQ1: 71 (14) $PC_{71}BM$: 29 (14)	$PC_{71}BM$	TQ1: 19 (3) $PC_{71}BM$: 81 (3)
STXM analysis outputs					
PTQ10:IDIC	Core-shell with high donor-acceptor intermixing	PTQ10	PTQ10: 62 (9) IDIC: 38 (9)	IDIC	[a] PTQ10: 24 (16) IDIC: 76 (4)

[a] The core-shell model reported in Holmes et al.[26] has been used to calculate the core composition from radial profiles.

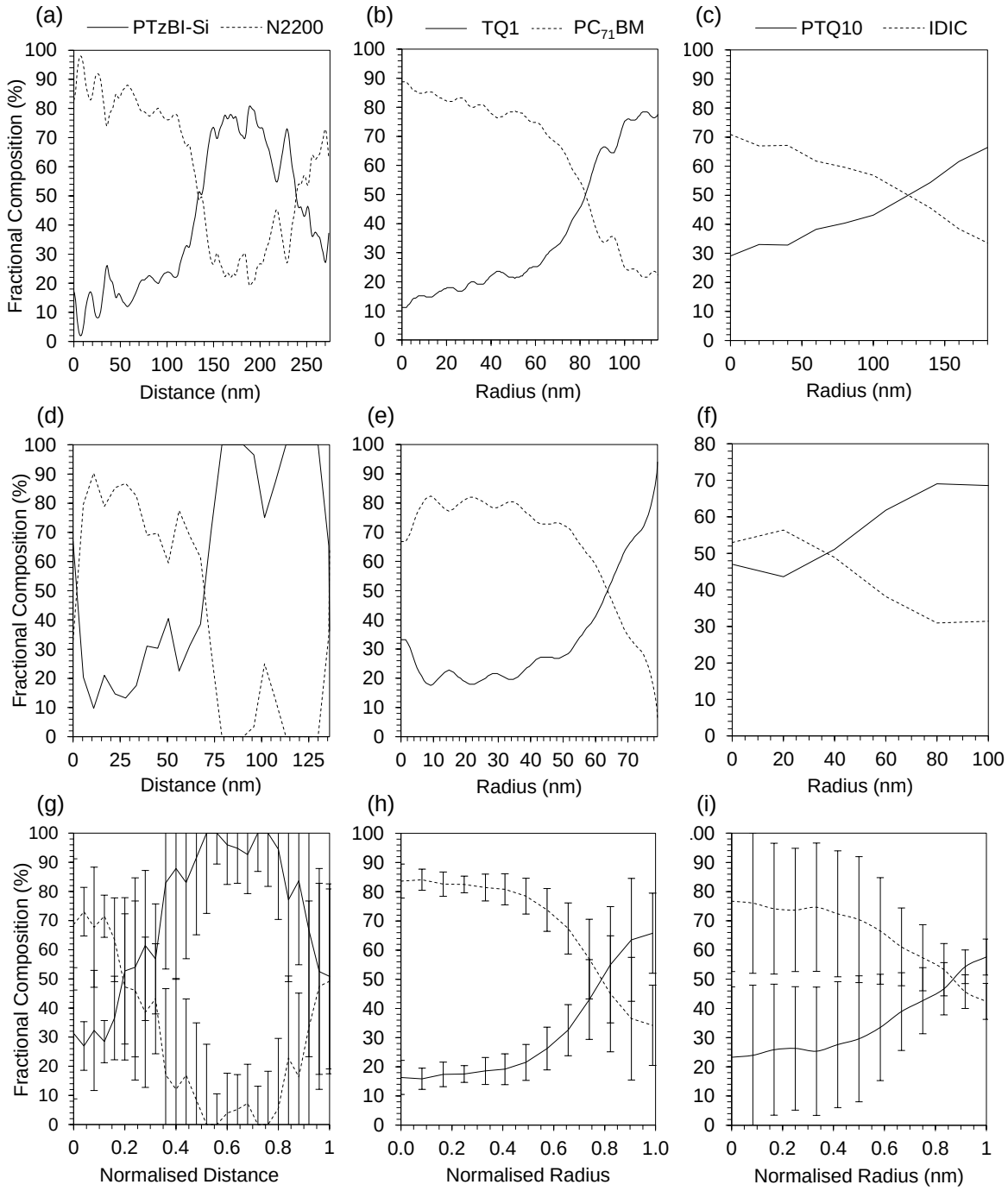

Figure 7. Line and radial composition profiles extracted from STEM EDX and STXM maps showing polymer donor (solid black) and NFA or fullerene acceptor (dashed black) fraction. (a,d,g) Line profiles (from STEM EDX maps) of a PTzBI-Si:N2200 nanoparticle in the 200-400 nm diameter size bin, 100-200 nm diameter size bin, and averaged (n = 9). (b,e,h) Radial profiles (from STEM EDX maps) of a TQ1:$PC_{71}BM$ nanoparticle in the 200-400 nm size bin, 100-200 nm diameter size bin, and averaged (n = 7). (c,f,i) Radial profiles (from STXM maps) of a PTQ10:IDIC nanoparticle in the 200-400 nm diameter size bin, 100-200 nm diameter size bin, and averaged (n = 10). The error bars represent standard deviation within each particle group.

Connection of Structure to Function

Photoluminescence experiments were performed to investigate the fluorescence quenching in the different composite donor-acceptor nanoparticles since it is a first indication of potential exciton dissociation and charge transfer from donor to acceptor.[53] Photoluminescence of pure donor nanoparticles (PTzBI-Si, TQ1 and PTQ10) were measured and compared to that of donor-acceptor composite nanoparticles (PTzBI-Si:N2200, TQ1:$PC_{71}BM$ and PTQ10:IDIC).

Firstly, for the PTzBI-Si:N2200 material system, the photoluminescence intensity of the donor material, PTzBI-Si, is high and only 32% is quenched by the N2200 acceptor in donor:acceptor nanoparticles (Figure 8a). This result indicates phase separation within the composite nanoparticles, with domains larger than the exciton diffusion length. This Janus morphology is visible in the STEM EDX images (Figure 2) which show off-centred cores composed mainly of PTzBI-Si. The photoluminescence result suggests that these domains are composed of almost pure PTzBI-Si, in agreement with the value calculated in Table 3.

In contrast, the TQ1:$PC_{71}BM$ composite nanoparticles present very low photoluminescence intensity compared to that of pure TQ1 nanoparticles (Figure 8b). Up to 97% of the TQ1 photoluminescence is quenched by the $PC_{71}BM$, indicating efficient electron transfer from the donor (TQ1) to the acceptor ($PC_{71}BM$) and spatial proximity between the two materials (within the exciton diffusion length).[54] Even though STEM EDX (Figure 3) and STXM images (Figure 5e-h) show a core-shell preferential morphology, with the acceptor material mainly in the core and the donor material mainly in the shell, photoluminescence experiments indicate that the shell is not purely composed of TQ1, but comprises also $PC_{71}BM$ since almost all TQ1 PL is quenched.

Concerning the PTQ10:IDIC composite nanoparticles, the photoluminescence intensity is also very weak with respect of the pure PTQ10 nanoparticles. The IDIC acceptor quenches up to 96% of PTQ10 photoluminescence (Figure 8c), which indicates also that the electron transfer is highly efficient in such composite donor:acceptor nanoparticles. This result indicates a proximity between the donor and the acceptor, within the exciton diffusion length (8-15 nm). STXM analysis shows a core-shell morphology (Figure 5i-l), with the acceptor material preferentially in the core, while STEM-EDX could not be relied upon due to suspected electron beam damage to the terminal F group (the element belonging to PTQ10 used as the fingerprint element), the result being STEM EDX maps indicating an intermixed morphology (Figure 4). The photoluminescence results shed further light on the true morphology of the nanoparticles.

Indeed, since the acceptor material IDIC must be spatially close to PTQ10 to extinct its fluorescence, the PTQ10 shell is likely to comprise IDIC molecules evenly spread to allow efficient charge transfer. Hence, the PTQ10:IDIC nanoparticle morphology comprises an intermixed PTQ10:IDIC shell and a core predominantly of IDIC.

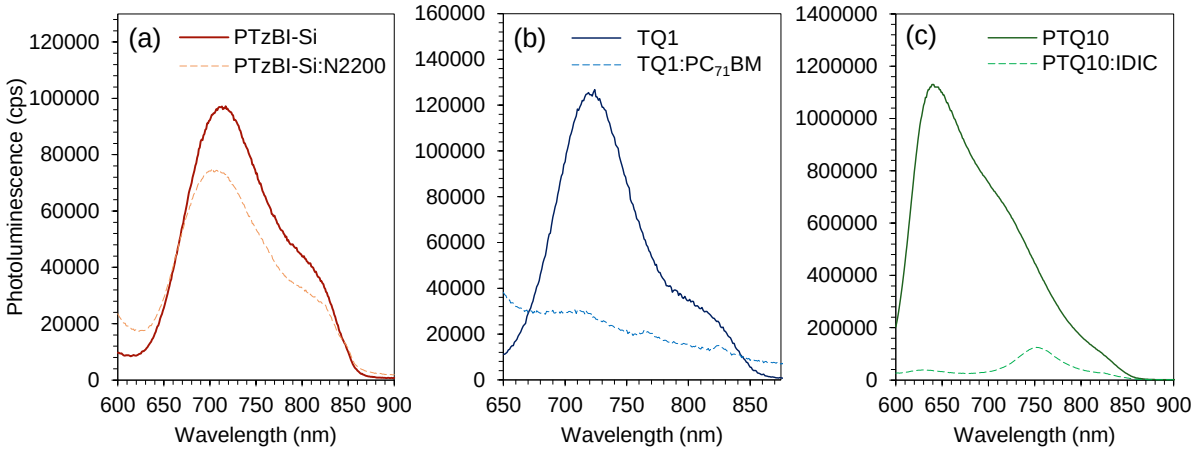

Figure 8. Steady-state photoluminescence spectra of (a) PTzBI-Si and PTzBI-Si:N2200 nanoparticles, (b) TQ1 and TQ1:$PC_{71}BM$ nanoparticles, and (c) PTQ10 and PTQ10:IDIC nanoparticles.

The performance of organic photovoltaic (OPV) devices is strongly dependent on the internal morphology of the composite nanoparticles as well as their sizes.[55] High efficiency OPV devices have been achieved with nanoparticles presenting intermixed morphology, generally obtained from the nanoprecipitation method, but also the miniemulsion method in several cases.[8,13,56,57] One can highlight the 7.5% PCE achieved for the PBQ-QF:ITIC system[8] from water-based dispersions and 4.3% for P3HT:ICBA[58] from alcohol-based dispersions. It has been shown in several studies by the Venkataraman group[59,60] that, if the surfactant is efficiently removed, the charge transport in OPV devices is not drastically affected and it is comparable to thin films deposited from organic solvents. The core-shell morphology of TQ1:$PC_{71}BM$, while presenting high photoluminescence quenching, and, as a consequence, high exciton dissociation rate, is not suitable for OPV devices if the core and shell domains are pure, which would cause electrons to be trapped in the core of the nanoparticles. Since the core and shell domains are $PC_{71}BM$-rich and TQ1-rich, respectively, charge percolation pathways exist for the transport of electrons and holes to their respective electrodes. It is also of note that upon thermal annealing, nano-bridges can be formed between the cores of the nanoparticles, improving therefore the device performance, as shown in our previous work.[27] Although, there remains a discrepancy between the performance of OPV devices fabricated from organic solvent (BHJ) and that of devices fabricated from nanoparticle dispersions, PCE 6%[34] and 2.5%[27] respectively (Table 4). Future work should target a nanoparticle shell with a 50:50 blend

of donor:acceptor, to improve charge transport and further close the gap between BHJ-OPV and NP-OPV performance. The morphology identified for PTzBI-Si:N2200 is Janus with an off-centred core of donor polymer, and with much larger phase separation than the other two systems studied. This type of nanoparticle morphology has potential to perform well in OPV devices, but only if an essential modification is performed reducing the nanoparticle size to <30 nm,[55] such that excitons have a shorter transport distance to reach an interface of donor and acceptor for efficient exciton quenching, which was not the case for the large nanoparticles studied in this report. While OPV devices fabricated from PTzBI-Si:N2200 in organic solvent can reach up to 11.8%,[21] we can aim at a NP-OPV device performance of 5.9%, 50% of that value, in alignment with the current trend for NP-OPV reaching 50% of the performance of BHJ-OPV for other material systems. The morphology identified for PTQ10:IDIC seems more adapted to OPV devices than the two others. On the one hand, high exciton dissociation rate is observed from photoluminescence experiments, indicating intermixing between the donor and the acceptor in the nanoparticle shell domain. This type of morphology is promising for OPV devices prepared from nanoparticle dispersions since this donor:acceptor material system can reach up to 12.7%[23] PCE when fabricated from organic solvent.

Table 4. Reported bulk heterojunction (BHJ) OPV device performance for the PTzBI-Si:N2200, TQ1:$PC_{71}BM$ and PTQ10:IDIC material systems, and forecasted nanoparticle (NP) OPV device performance based on current trends. *Predicted values.

Donor: Acceptor System	OPV PCE	
	BHJ	**NP**
PTzBI-Si:N2200	11.8%[21]	5.9%*
TQ1:$PC_{71}BM$	6%[34]	2.5%[27]
PTQ10:IDIC	12.7%[23]	6.4%*

Future Directions for Ideal Nanostructures

Customisable waterborne nanoparticulate colloidal dispersions are highly sought-after in multiple disciplines. For nanomedicines, the ideal structure for drug delivery is core-shell. For example, hybrid bio-nanoconstructs have a drug-loaded core, a biodegradable polymer shell and surface-functionalised peptides. In the emerging field of photocatalysis and hydrogen generation by organic nanoparticles, it has been shown that a molecularly intermixed nanostructure is more favourable than a core-shell nanostructure for improving the hydrogen production rate.[13] In the field of organic photovoltaics, core-shell morphologies can produce reasonable efficiencies if the nanoparticle shell composition is a blend of donor and acceptor, to avoid charges being trapped in the core. The highest efficiencies for nanoparticulate based

OPV devices are reported for molecularly intermixed structures, since this morphology ensures high exciton dissociation rates and percolation pathways for the charges. Nanoengineering strategies for producing Janus morphologies for applications in OPV have only recently been reported.[30,61] It is theorised that the Janus nanoparticle morphology could become the ideal morphology for OPV (and for photocatalytic applications) because Janus nanoparticles of small diameters (<30 nm) could combine high exciton dissociation rate and perfect conduction pathways for both charges.[12] Therefore, the OPV field needs strategies to carefully tune the nanomorphology of donor-acceptor nanoparticles and powerful techniques, such as STEM EDX, to confirm their morphologies which will define the device performance.

Conclusions

Here we report the sub-4 nm mapping of composition in organic semiconductor binary blend nanoparticles with STEM EDX. Although STEM EDX has been available for several years, sub-4 nm precision elemental mapping at low accelerating voltage (60 kV) has not previously been reported for donor-acceptor blends to determine the internal morphology of nanoparticles as small as 30 nm in diameter. We provide qualitative and quantitative mapping of two new high performance polymer donor : NFA material systems (PTzBI-Si:N2200 and PTQ10:IDIC), and one long-established polymer donor : fullerene acceptor system (TQ1:$PC_{71}BM$). The ability to resolve the internal structure of nanoparticles as small as 30 nm in diameter – information that was previously inaccessible – is highly relevant to OPV device applications. This non-synchrotron-based mapping technique is compared to the synchrotron-based STXM technique, with an inferior spatial resolution limit (by two orders of magnitude). The chemical identification and quantification of such materials with sub-4 nm resolution is a welcome addition to the nano-characterisation toolbox, and is available for making breakthroughs in organic electronics, photocatalysis and nanomedicine.

Conflicts of Interest

There are no conflicts of interest to declare.

Acknowledgements

The authors acknowledge the technical and scientific assistance of Sydney Microscopy & Microanalysis, the University of Sydney node of Microscopy Australia. We further thank the support of the University of Sydney Core Research Facilities. The PolLux end station (X07DA) at the Swiss Light Source synchrotron was financed by the German Minister für Bildung und

Forschung (BMBF) through contracts 05K16WED and 05K19WE2. This research used resources of the Advanced Light Source, which is a DOE Office of Science User Facility under contract no. DE-AC02-05CH11231. The authors thank support staff at the Advanced Light Source synchrotron. I.P recognises the support from the Swedish Research Council via an international postdoc grant (No. 2020-00589). N.P.H. acknowledges travel funding provided by the International Synchrotron Access Program (ISAP) managed by the Australian Synchrotron, part of ANSTO, and funded by the Australian Government. N.P.H. acknowledges the University of Tokyo Institute of Industrial Science (IIS) for funding an IIS Invited International Researcher travel grant. The authors acknowledge the support provided by the ANR through the WATER-PV project N°ANR-20-CE05-0002-01. We acknowledge the support from the LIGHT S&T Graduate Program (PIA3 Investment for the Future, ANR-17-EURE-0027).

Supplementary Material

Supplementary material is available for this article in the online version. Additional STEM EDX and STXM maps for PTzBI-Si:N2200, TQ1:$PC_{71}BM$ and PTQ10:IDIC nanoparticle systems. NEXAFS spectra of all organic semiconductors. EDX spectra of PTzBI-Si:N2200, TQ1:$PC_{71}BM$ and PTQ10:IDIC nanoparticles. Calculation of the resolution limit of the STEM EDX mapping. Comparison of STEM EDX to STXM technique capability. Nanoparticle shell thickness vs diameter analysis. Post-EDX mapping STEM showing minimal carbon deposition during STEM EDX mapping. UV-Vis absorbance spectra of nanoparticle dispersions.

References

(1) Price, M. B.; Hume, P. A.; Ilina, A.; Wagner, I.; Tamming, R. R.; Thorn, K. E.; Jiao, W.; Goldingay, A.; Conaghan, P. J.; Lakhwani, G.; et al. Free Charge Photogeneration in a Single Component High Photovoltaic Efficiency Organic Semiconductor. *Nat. Commun.* **2022**, *13*, 2827.

(2) Clarke, T. M.; Durrant, J. R. Charge Photogeneration in Organic Solar Cells. *Chem. Rev.* **2010**, *110* (11), 6736–6767.

(3) Björström Svanström, C. M.; Rysz, J.; Bernasik, A.; Budkowski, A.; Zhang, F.; Inganäs, O.; Andersson, M. R.; Magnusson, K. O.; Benson-Smith, J. J.; Nelson, J.; et al. Device Performance of APFO-3/PCBM Solar Cells with Controlled Morphology. *Adv. Mater.* **2009**, *21* (43), 4398–4403.

(4) Zhao, F.; Wang, C.; Zhan, X. Morphology Control in Organic Solar Cells. *Adv. Energy Mater.* **2018**, *1703147*, 1–34.

(5) Holmes, N. P.; Marks, M.; Cave, J. M.; Feron, K.; Barr, M. G.; Fahy, A.; Sharma, A.; Pan, X.; Kilcoyne, D. A. L.; Zhou, X.; et al. Engineering Two-Phase and Three-Phase Microstructures from Water-Based Dispersions of Nanoparticles for Eco-Friendly Polymer Solar Cell Applications. *Chem. Mater.* **2018**, *30*, 6521−6531.

(6) Holmes, N. P.; Nicolaidis, N.; Feron, K.; Barr, M.; Burke, K. B.; Al-Mudhaffer, M.; Sista, P.; Kilcoyne, A. L. D.; Stefan, M. C.; Zhou, X.; et al. Probing the Origin of Photocurrent in Nanoparticulate Organic Photovoltaics. *Sol. Energy Mater. Sol. Cells* **2015**, *140*, 412–421.

(7) Holmes, N. P.; Ulum, S.; Sista, P.; Burke, K. B.; Wilson, M. G.; Stefan, M. C.; Zhou, X.; Dastoor, P. C.; Belcher, W. J. The Effect of Polymer Molecular Weight on P3HT:PCBM Nanoparticulate Organic Photovoltaic Device Performance. *Sol. Energy Mater. Sol. Cells* **2014**, *128*, 369–377.

(8) Xie, C.; Heumüller, T.; Gruber, W.; Tang, X.; Classen, A.; Schuldes, I.; Bidwell, M.; Späth, A.; Fink, R. H.; Unruh, T.; et al. Overcoming Efficiency and Stability Limits in Water-Processing Nanoparticular Organic Photovoltaics by Minimizing Microstructure Defects. *Nat. Commun.* **2018**, *9*, 5335.

(9) Chambon, S.; Schatz, C.; Sébire, V.; Pavageau, B.; Wantz, G.; Hirsch, L. Organic Semiconductor Core–Shell Nanoparticles Designed through Successive Solvent Displacements. *Mater. Horizons* **2014**, *1* (4), 431–438.

(10) Holmes, A.; Deniau, E.; Lartigau-dagron, C.; Bousquet, A.; Chambon, S.; Holmes, N. P. Review of Waterborne Organic Semiconductor Colloids for Photovoltaics. *ACS Nano* **2021**, *15* (3), 3927–3959.

(11) Cui, Y.; Xu, Y.; Yao, H.; Bi, P.; Hong, L.; Zhang, J.; Zu, Y.; Zhang, T.; Qin, J.; Ren, J.; et al. Single-Junction Organic Photovoltaic Cell with 19% Efficiency. *Adv. Mater.* **2021**, *33*, 2102420.

(12) Holmes, N. P.; Chambon, S.; Holmes, A.; Xu, X.; Hirakawa, K.; Deniau, E.; Lartigau-Dagron, C.; Bousquet, A. Organic Semiconductor Colloids: From the Knowledge Acquired in Photovoltaics to the Generation of Solar Hydrogen Fuel. *Curr. Opin.*

Colloid Interface Sci. **2021**, *56*, 101511.

(13) Kosco, J.; Bidwell, M.; Cha, H.; Martin, T.; Howells, C. T.; Sachs, M.; Anjum, D. H.; Gonzalez Lopez, S.; Zou, L.; Wadsworth, A.; et al. Enhanced Photocatalytic Hydrogen Evolution from Organic Semiconductor Heterojunction Nanoparticles. *Nat. Mater.* **2020**, *19* (5), 559–565.

(14) Pavliuk, M. V; Wrede, S.; Liu, A.; Brnovic, A.; Wang, S. Preparation, Characterization, Evaluation and Mechanistic Study of Organic Polymer Nano-Photocatalysts for Solar Fuel Production. *Chem. Soc. Rev.* **2022**, *51*, 6909–6935.

(15) Duan, L.; Elumalai, N. K.; Zhang, Y.; Uddin, A. Progress in Non-Fullerene Acceptor Based Organic Solar Cells. *Sol. Energy Mater. Sol. Cells* **2019**, *193*, 22–65.

(16) Sun, H.; Liu, T.; Yu, J.; Lau, T.-K.; Zhang, G.; Zhang, Y.; Su, M.; Tang, Y.; Ma, R.; Liu, B.; et al. A Monothiophene Unit Incorporating Both Fluoro and Ester Substitution Enabling High-Performance Donor Polymers for Non-Fullerene Solar Cells with 16.4% Efficiency. *Energy Environ. Sci.* **2019**, *12*, 3328–3337.

(17) Fan, Q.; An, Q.; Lin, Y.; Xia, Y.; Li, Q.; Zhang, M.; Su, W.; Peng, W.; Zhang, C.; Liu, F.; et al. Over 14% Efficiency All-Polymer Solar Cells Enabled by a Low Bandgap Polymer Acceptor with Low Energy Loss and Efficient Charge Separation. *Energy Environ. Sci.* **2020**, *13* (12), 5017–5027.

(18) Du, X.; Heumueller, T.; Gruber, W.; Classen, A.; Unruh, T.; Li, N.; Brabec, C. J. Efficient Polymer Solar Cells Based on Non-Fullerene Acceptors with Potential Device Lifetime Approaching 10 Years. *Joule* **2019**, *3* (1), 215–226.

(19) de la Perrelle, J. M.; Dolan, A.; Milsom, E. R.; Small, T. D.; Metha, G. F.; Pan, X.; Andersson, M. R.; Huang, D. M.; Kee, T. W. Red-Light-Mediated Photocatalytic Hydrogen Evolution by Hole Transfer from Non-Fullerene Acceptor Y6. *J. Phys. Chem. C* **2022**, *126* (34), 14518–14528.

(20) Fan, B.; Ying, L.; Zhu, P.; Pan, F.; Liu, F.; Chen, J.; Huang, F.; Cao, Y. All-Polymer Solar Cells Based on a Conjugated Polymer Containing Siloxane-Functionalized Side Chains with Efficiency over 10%. *Adv. Mater.* **2017**, *29*, 1703906.

(21) Zhu, L.; Zhong, W.; Qiu, C.; Lyu, B.; Zhou, Z.; Zhang, M.; Song, J.; Xu, J.; Wang, J.; Ali, J.; et al. Aggregation-Induced Multilength Scaled Morphology Enabling 11.76%

Efficiency in All-Polymer Solar Cells Using Printing Fabrication. *Adv. Mater.* **2019**, *31*, 1902899.

(22) Lin, Y.; He, Q.; Zhao, F.; Huo, L.; Mai, J.; Lu, X.; Su, C. J.; Li, T.; Wang, J.; Zhu, J.; et al. A Facile Planar Fused-Ring Electron Acceptor for as-Cast Polymer Solar Cells with 8.71% Efficiency. *J. Am. Chem. Soc.* **2016**, *138*, 2973–2976.

(23) Sun, C.; Pan, F.; Bin, H.; Zhang, J.; Xue, L.; Qiu, B.; Wei, Z.; Zhang, Z.-G.; Li, Y. A Low Cost and High Performance Polymer Donor Material for Polymer Solar Cells. *Nat. Commun.* **2018**, *9* (1), 743.

(24) Wu, Y.; Zheng, Y.; Yang, H.; Sun, C.; Dong, Y.; Cui, C.; Yan, H.; Li, Y. Rationally Pairing Photoactive Materials for High-Performance Polymer Solar Cells with Efficiency of 16.53%. *Sci. China Chem.* **2020**, *63* (2), 265–271.

(25) Ulum, S.; Holmes, N.; Barr, M.; Kilcoyne, A. L. D.; Gong, B. Bin; Zhou, X.; Belcher, W.; Dastoor, P. The Role of Miscibility in Polymer:Fullerene Nanoparticulate Organic Photovoltaic Devices. *Nano Energy* **2013**, *2*, 897–905.

(26) Holmes, N. P.; Burke, K. B.; Sista, P.; Barr, M.; Magurudeniya, H. D.; Stefan, M. C.; Kilcoyne, A. L. D.; Zhou, X.; Dastoor, P. C.; Belcher, W. J. Nano-Domain Behaviour in P3HT:PCBM Nanoparticles, Relating Material Properties to Morphological Changes. *Sol. Energy Mater. Sol. Cells* **2013**, *117*, 437–445.

(27) Holmes, N. P.; Marks, M.; Kumar, P.; Kroon, R.; Barr, M. G.; Nicolaidis, N.; Feron, K.; Pivrikas, A.; Fahy, A.; Diaz De Zerio Mendaza, A.; et al. Nano-Pathways: Bridging the Divide Between Water-Processable Nanoparticulate and Bulk Heterojunction Organic Photovoltaics. *Nano Energy* **2016**, *19*, 495–510.

(28) Holmes, N. P.; Vaughan, B.; Williams, E. L.; Kroon, R.; Anderrson, M. R.; Kilcoyne, A. L. D.; Sonar, P.; Zhou, X.; Dastoor, P. C.; Belcher, W. J. Diketopyrrolopyrrole-Based Polymer:Fullerene Nanoparticle Films with Thermally Stable Morphology for Organic Photovoltaic Applications. *MRS Commun.* **2017**, *7* (1), 67–73.

(29) Barr, M. G.; Chambon, S.; Fahy, A.; Jones, T. W.; Marcus, M. A.; Kilcoyne, A. L. D.; Dastoor, P. C.; Griffith, M. J.; Holmes, N. P. Nanomorphology of Eco-Friendly Colloidal Inks, Relating Non-Fullerene Acceptor Surface Energy to Structure Formation. *Mater. Chem. Front.* **2021**, *5* (5), 2218–2233.

(30) Du, Y.; Li, Y.; Aftenieva, O.; Tsuda, T.; Formanek, P.; König, T. A. F.; Synytska, A. High Yield Synthesis of Water-Processable Donor:Acceptor Janus Nanoparticles with Tuned Internal Morphology and Highly Efficient Charge Separation/Transfer. *Adv. Opt. Mater.* **2022**, *10*, 2101922.

(31) D'Olieslaeger, L.; Pfannmöller, M.; Fron, E.; Cardinaletti, I.; Van Der Auweraer, M.; Van Tendeloo, G.; Bals, S.; Maes, W.; Vanderzande, D.; Manca, J.; et al. Tuning of PCDTBT:PC71BM Blend Nanoparticles for Eco-Friendly Processing of Polymer Solar Cells. *Sol. Energy Mater. Sol. Cells* **2017**, *159*, 179–188.

(32) Pfannmöller, M.; Flügge, H.; Benner, G.; Wacker, I.; Sommer, C.; Hanselmann, M.; Schmale, S.; Schmidt, H.; Hamprecht, F. A.; Rabe, T.; et al. Visualizing a Homogeneous Blend in Bulk Heterojunction Polymer Solar Cells by Analytical Electron Microscopy. *Nano Lett.* **2011**, *11* (8), 3099–3107.

(33) Chamberlain, T. W.; Biskupek, J.; Skowron, S. T.; Bayliss, P. A.; Bichoutskaia, E.; Kaiser, U.; Khlobystov, A. N. Isotope Substitution Extends the Lifetime of Organic Molecules in Transmission Electron Microscopy. *Small* **2015**, *11* (5), 622–629.

(34) Wang, E.; Hou, L.; Wang, Z.; Hellström, S.; Zhang, F.; Inganäs, O.; Andersson, M. R. An Easily Synthesized Blue Polymer for High-Performance Polymer Solar Cells. *Adv. Mater.* **2010**, *22* (46), 5240–5244.

(35) Hummelen, J. C.; Knight, B. W.; Lepeq, F.; Wudl, F.; Yao, J.; Wilkins, C. L. Preparation and Characterization of Fulleroid and Methanofullerene Derivatives. *J. Org. Chem.* **1995**, *60* (3), 532–538.

(36) He, X.; Collins, B. A.; Watts, B.; Ade, H.; McNeill, C. R. Studying Polymer/Fullerene Intermixing and Miscibility in Laterally Patterned Films with X-Ray Spectromicroscopy. *Small* **2012**, *8*, 1920–1927.

(37) Frommherz, U.; Raabe, J.; Watts, B.; Stefani, R.; Ellenberger, U. Higher Order Suppressor (HOS) for the PolLux Microspectroscope Beamline at the Swiss Light Source SLS. *AIP Conf. Proc.* **2010**, *1234*, 429–432.

(38) Kilcoyne, A. L. D.; Tyliszczak, T.; Steele, W. F.; Fakra, S.; Hitchcock, P.; Franck, K.; Anderson, E.; Harteneck, B.; Rightor, E. G.; Mitchell, G. E.; et al. Interferometer-Controlled Scanning Transmission X-Ray Microscopes at the Advanced Light Source.

J. Synchrotron Radiat. **2003**, *10*, 125–136.

(39) Flechsig, U.; Quitmann, C.; Raabe, J.; Böge, M.; Fink, R.; Ade, H. The PolLux Microspectroscopy Beam Line at the Swiss Light Source. *AIP Conf. Proc.* **2007**, *879*, 505–508.

(40) Raabe, J.; Tzvetkov, G.; Flechsig, U.; Böge, M.; Jaggi, A.; Sarafimov, B.; Vernooij, M. G. C.; Huthwelker, T.; Ade, H.; Kilcoyne, D.; et al. PolLux: A New Facility for Soft x-Ray Spectromicroscopy at the Swiss Light Source. *Rev. Sci. Instrum.* **2008**, *79*, 113704.

(41) McNeill, C. R.; Watts, B.; Thomsen, L.; Belcher, W. J.; Greenham, N. C.; Dastoor, P. C. Nanoscale Quantitative Chemical Mapping of Conjugated Polymer Blends. *Nano Lett.* **2006**, *6*, 1202–1206.

(42) Landfester, K.; Montenegro, R.; Scherf, U.; Güntner, R.; Asawapirom, U.; Patil, S.; Neher, D.; Kietzke, T. Semiconducting Polymer Nanospheres in Aqueous Dispersion Prepared by a Miniemulsion Process. *Adv. Mater.* **2002**, *14* (9), 651–655.

(43) Egerton, R. F. Radiation Damage to Organic and Inorganic Specimens in the TEM. *Micron* **2019**, *119*, 72–87.

(44) Buban, J. P.; Ramasse, Q.; Gipson, B.; Browning, N. D.; Stahlberg, H. High-Resolution Low-Dose Scanning Transmission Electron Microscopy. *J. Electron Microsc. (Tokyo).* **2010**, *59* (2), 103–112.

(45) Leijten, Z. J. W. A.; Keizer, A. D. A.; De With, G.; Friedrich, H. Quantitative Analysis of Electron Beam Damage in Organic Thin Films. *J. Phys. Chem. C* **2017**, *121* (19), 10552–10561.

(46) Shuman, H.; Kruit, P. Quantitative Data Processing of Parallel Recorded Electron Energy-Loss Spectra with Low Signal to Background. *Rev. Sci. Instrum.* **1985**, *56* (2), 231–239.

(47) Fabiano, S.; Himmelberger, S.; Drees, M.; Chen, Z.; Altamimi, R. M.; Salleo, A.; Loi, M. A.; Facchetti, A. Charge Transport Orthogonality in All-Polymer Blend Transistors, Diodes, and Solar Cells. *Adv. Energy Mater.* **2014**, *4*, 1301409.

(48) Kraka, E.; Cremer, D. Characterization of CF Bonds with Multiple-Bond Character: Bond Lengths, Stretching Force Constants, and Bond Dissociation Energies.

ChemPhysChem **2009**, *10*, 686 – 698.

(49) Egerton, R. F. Choice of Operating Voltage for a Transmission Electron Microscope. *Ultramicroscopy* **2014**, *145*, 85–93.

(50) Brumboiu, I. E.; Anselmo, A. S.; Brena, B.; Dzwilewski, A.; Svensson, K.; Moons, E. Near-Edge X-Ray Absorption Fine Structure Study of the C60-Derivative PCBM. *Chem. Phys. Lett.* **2013**, *568–569*, 130–134.

(51) Pan, X.; Sharma, A.; Gedefaw, D.; Kroon, R.; Diaz de Zerio, A.; Holmes, N. P.; Kilcoyne, A. L. D.; Barr, M. G.; Fahy, A.; Marks, M.; et al. Environmentally Friendly Preparation of Nanoparticles for Organic Photovoltaics. *Org. Electron.* **2018**, *59*, 432–440.

(52) Andersen, T. R.; Larsen-Olsen, T. T.; Andreasen, B.; Böttiger, A. P. L.; Carlé, J. E.; Helgesen, M.; Bundgaard, E.; Norrman, K.; Andreasen, J. W.; Jørgensen, M.; et al. Aqueous Processing of Low-Band-Gap Polymer Solar Cells Using Roll-to-Roll Methods. *ACS Nano* **2011**, *5*, 4188–4196.

(53) Kietzke, T.; Neher, D.; Kumke, M.; Montenegro, R.; Landfester, K.; Scherf, U. A Nanoparticle Approach to Control the Phase Separation in Polyfluorene Photovoltaic Devices. *Macromolecules* **2004**, *37* (13), 4882–4890.

(54) Shaw, P. E.; Ruseckas, A.; Samuel, I. D. W. Exciton Diffusion Measurements in Poly(3-Hexylthiophene). *Adv. Mater.* **2008**, *20*, 3516–3520.

(55) Colberts, F. J. M.; Wienk, M. M.; Janssen, R. A. J. Aqueous Nanoparticle Polymer Solar Cells: Effects of Surfactant Concentration and Processing on Device Performance. *ACS Appl. Mater. Interfaces* **2017**, *9*, 13380−13389.

(56) Xie, C.; Liang, S.; Zhang, G.; Li, S. Water-Processed Organic Solar Cell with Efficiency Exceeding 11%. *Polymers (Basel).* **2022**, *14*, 4229.

(57) Manger, F.; Fischer, K.; Marlow, P.; Röhm, H.; Sprau, C.; Colsmann, A. Iodine-Stabilized Organic Nanoparticle Dispersions for the Fabrication of 10% Efficient Non-Fullerene Solar Cells. *Adv. Energy Mater.* **2022**, *2202820*, 1–7.

(58) Xie, C.; Tang, X.; Berlinghof, M.; Langner, S.; Chen, S.; Späth, A.; Li, N.; Fink, R. H.; Unruh, T.; Brabec, C. J. Robot-Based High-Throughput Engineering of Alcoholic Polymer: Fullerene Nanoparticle Inks for an Eco-Friendly Processing of Organic Solar

Cells. *ACS Appl. Mater. Interfaces* **2018**, *10* (27), 23225–23234.

(59) Bag, M.; Gehan, T. S.; Algaier, D. D.; Liu, F.; Nagarjuna, G.; Lahti, P. M.; Russell, T. P.; Venkataraman, D. Efficient Charge Transport in Assemblies of Surfactant-Stabilized Semiconducting Nanoparticles. *Adv. Mater.* **2013**, *25*, 6411–6415.

(60) Han, X.; Bag, M.; Gehan, T. S.; Venkataraman, D.; Maroudas, D. Analysis of Hole Transport in Thin Films and Nanoparticle Assemblies of Poly(3-Hexylthiophene). *Chem. Phys. Lett.* **2014**, *610–611*, 273–277.

(61) Holmes, A.; Laval, H.; Schmutz, M.; Blanc, S.; Allouche, J.; Watts, B.; Wantz, G.; Holmes, N. P.; Hirakawa, K.; Deniau, E.; et al. Janus Organic Semiconductor Nanoparticles Prepared by Simple Nanoprecipitation. *Mater. Today Chem.* **2022**, *26*, 101229.